

# Velocity model building in the major basins of the eastern Mediterranean Sea for imaging regional prospectivity

Ahmed El-Bassiony<sup>1</sup>, Jyoti Kumar<sup>1</sup>, and Tony Martin<sup>2</sup>

<https://doi.org/10.1190/tle37070519.1>

## Abstract

Hydrocarbon prospectivity in the eastern Mediterranean is challenged by the presence of the Messinian salt layer, which varies in complexity across the area. The macro salt layer geometry itself varies from the deep abyssal planes in the middle of two major basins (the Herodotus and Levant basins), where it shows simple top and base relief to more complicated geometries near the continental salt-free shelf. Building depth velocity models for imaging the eastern Mediterranean basins requires accurate determination of the complex salt top and base, as well as accurate estimation of their velocities. Since 2006, many 2D and 3D megasurveys using conventional and dual-sensor acquisitions have been carried out across the area. Regional and relatively simple velocity models are used to image the Messinian salt layer extensions from offshore West Egypt to offshore Lebanon, passing by the Cypriot waters and the Eratosthenes Seamount. The data acquired include shallow and deepwater surveys, and technologies such as full-waveform inversion are applied to produce high-resolution images for the shallow post-Messinian section. Shallow-water imaging challenges such as acquisition footprint issues and low-angle illumination are solved by imaging with multiples using dual-sensor acquisition data. The Messinian salt layer is modeled with a simple constant regional velocity, while the pre-Messinian section is modeled with a simple combination of velocity gradient models. The regional model-building scheme introduces a good correction for the pre-Messinian structure and provides reliable multivalent data ready for outlining new prospects.

## Introduction

The offshore eastern Mediterranean region has received increased international interest in the last decade for its hydrocarbon potential. Discoveries in offshore Egypt, Israel, and Cyprus have revealed huge reservoirs. The main challenges in imaging the subsurface structures are the presence of the Messinian salt layer and its variable complexities. Additionally, the pre-Messinian layers can show a degree of complexity, making the process of optimizing the depth velocity models limited by the acquisition geometry and the availability of well information. Since 2008, PGS has used its dual-sensor technology on a number of 2D lines offshore Cyprus. This was followed by a large 2D megasurvey project offshore Cyprus, then offshore Israel, Lebanon, Egypt, and recently Greece. The geologic setting of the eastern Mediterranean is well studied from the regional perspective and from the limited well information. The Herodotus and Levant basins have similar stratigraphic conditions and many similarities in their velocity and density profiles. The salt layer complexity will be addressed in the following sections. It will show simple compressive nature away from the Nile cone

but with a lot of intrasalt sediments from different drainage systems. To deal with this complexity, a simple constant velocity is included that can average the whole salt and intrasalt velocities. This means the effect of the salt layer as a macro unit can be compensated for in the imaging process. Another form of complexity exists where the salt layer starts to vanish close to the stable continental shelves, so accurate interpretation of the diapiric nature of the salt layer is essential to image stable pre-Messinian structures beneath. These two complex salt scenarios exist throughout the extension from the Herodotus Basin to the Levant Basin, with the Eratosthenes Seamount (ESM) dissecting the Messinian salt offshore Cyprus. Presented here are different strategies for building 2D and 3D subsurface velocity models in the different basins across the eastern Mediterranean. Methodologies will include the three major divisions of the Plio-Pleistocene section or simply the postsalt, the Messinian salt, and the pre-Messinian section that includes the Miocene-Paleogene section and the carbonate platform.

## Geologic settings

The eastern Mediterranean includes two major basins of nearly the same age, the Levant and the Herodotus. They share the same sediment type with the same thicknesses, but the Herodotus Basin is approximately twice the size of the Levant. The Levant Basin is located offshore Palestine, Israel, and Lebanon. It forms a northeast-trending depression about 1.5–2.0 km deep (Figure 1). Its origin is regarded as a response to several phases of rifting during the Early Triassic–Late Cretaceous (Gradmann et al., 2005), with subsequent subsidence driven by post-Cretaceous thermal subsidence and loading by Nile Delta sediments (Gardosh and Druckman, 2006). The bedrock is of Triassic age and has proved to be of highly attenuated continental crust origin (Ben-Avraham et al., 2002). The Levant Basin contains more than 14 km of Mesozoic–Cenozoic successions, including up to 2 km of Messinian salt and 0.5–1.2 km of Plio-Pleistocene (Druckman et al., 1995; Ben-Avraham et al., 2002; Netzeband et al., 2006). Toward the southeastern corner of the basin, the Plio-Pleistocene section is dominated by sediment forming the distal, northeast part of the Nile Delta (Loncke et al., 2006; Macgregor, 2012). In the north, along the Levant Margin, Plio-Pleistocene sediment was probably derived from drainage systems along the eastern basin margin, originating from the uplifted mountain ranges associated with the growth of the Dead Sea transform zone (Figure 1).

Suitable Cenozoic sandstone reservoirs are expected in the basal Plio-Pleistocene, intra-Messinian, and Middle to Lower Cenozoic successions. Cretaceous reservoirs may include both sandstones and limestones (including carbonate reefs). Jurassic reservoirs may also consist of sandstones and limestones, including

<sup>1</sup>PGS-Imaging, Cairo, Egypt. E-mail: [ahmed.elbassiony@pgs.com](mailto:ahmed.elbassiony@pgs.com); [jyoti.kumar@pgs.com](mailto:jyoti.kumar@pgs.com).

<sup>2</sup>PGS-Imaging, Weybridge, UK. E-mail: [tony.martin@pgs.com](mailto:tony.martin@pgs.com).

fractured dolomites and oolitic limestones. The oldest potential reservoirs are in the Triassic sandstones. Impermeable sedimentary rocks that could provide top and/or lateral seals are found in the Messinian salt, shales, and marls of the Paleogene, Neogene, Cretaceous, and Jurassic as well as Triassic evaporates (Roberts and Peace, 2007). The traps are stratigraphic and structural, such as anticline and pinch outs.

The Herodotus Basin is a 3 km deep depression with a north-east trend that represents an old slab of the Early Mesozoic Neo-Tethys Ocean (Figure 1). The basin is bounded on the north by the Mediterranean Ridge, on the northeast by the west portion of the Cyprus Arc, and on the south by the cone of the Nile Delta. The ESM, a fragment of continental crust (Robertson, 1998), forms the eastern limit of the Herodotus Basin, representing the boundary between the cone of the Nile Delta, the Herodotus Basin, and the Levant Basin. The Herodotus Basin contains more than 7 km of Mesozoic–Cenozoic succession (Voogd and Truffert, 1992; Garfunkel, 1998), which is overlain by up to 2–3 km of

Messinian salt and 1–4 km of Plio-Pleistocene overburden (Garfunkel, 1998; Aal et al., 2000; Loncke et al., 2006). Over time, the size of the basin has diminished as the Nile cone progrades into the basin. As a result, the sediments accreted to the Mediterranean Ridge (Elia et al., 2013). The bedrock of the basin is oceanic crust of Triassic age. Chronologically, the sediments are divided into Mesozoic and Paleogene sediments, pre-Messinian sediments (Miocene), Messinian evaporites, and Plio-Pleistocene–Quaternary sediments. Figure 1b shows the pre-Messinian sediments including calcareous siltstones, fossiliferous micrites of Serravallian age, sapropels of Tortonian age, and graded biomicrites and bio-arenites of Tortonian–Messinian age.

The Messinian evaporates originated during the closing of Gibraltar, with evaporate thicknesses reaching 3 km. The structure of the evaporites can be domal form due to either syndepositional folding or diapiric movements. The Plio-Pleistocene–Quaternary deposits consist of sediments rich in carbonate material. These deposits are laminated and rich in organic material, sapropels,

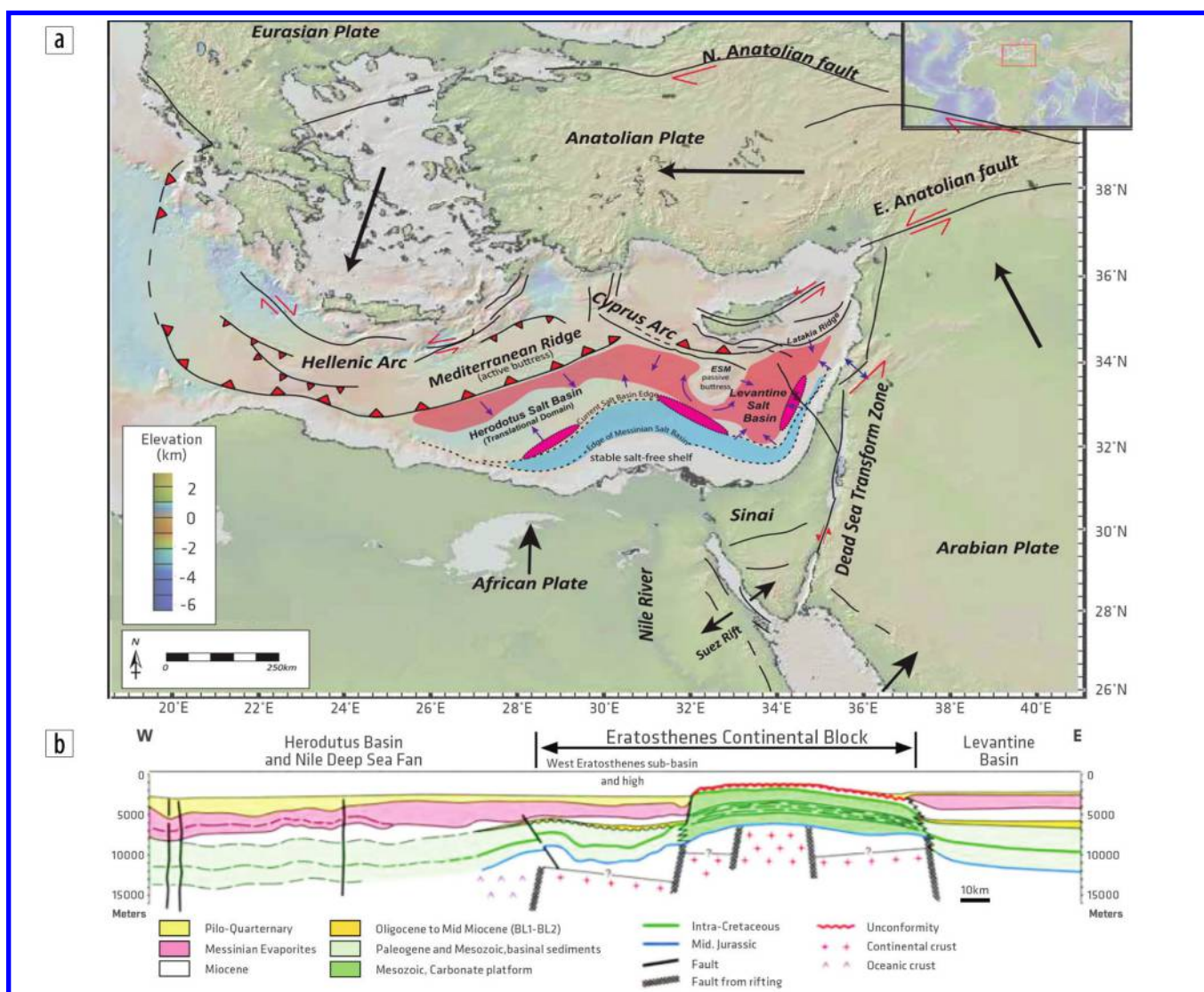


**Figure 1.** (a) Eastern Mediterranean structural elements map showing the two major basins (Levant and Herodotus) after Robertson and Mountrakis (2006) and Gardosh et al. (2008). (b) East-west profile showing stratigraphic sequence across the ESM, with the Levant Basin to the east and the Herodotus Basin to the west (Elia et al., 2013).

and sand turbidites. The sand turbidites were classified into three classes mainly originating from the Nile cone containing smectite, the African plate carbonate, and from the Anatolian plate rise. The sands of the first class of the Nile turbidites were transported through the five main Nile submarine channels, which were considered a primary target for hydrocarbon prospectivity in the early stages of the Nile Delta prospectivity efforts.

### Regional velocity-model-building methodology in the eastern Mediterranean

The earth-model-building (velocity-model-building) approach starts with the water velocity layer. Usually, a scan of constant velocities is performed to check the variation of velocity at different water depths. The optimum velocity that flattens the common-image gathers (CIG) in depth at the water bottom (WB) will be noted against the depth of the WB. A  $V_0 + kZ$  function is generated, where  $V_0$  is a starting velocity,  $Z$  is the depth of the WB, and  $k$  is the gradient that determines the change in velocity spatially. Some surveys include temperature-salinity (TS) curves measured at different locations across the study area. The TS curves are utilized whenever the salinity of the water changes (i.e., offshore Nile Delta environment) or the temperature significantly changes from shallow to deep water. For deepwater velocity models, a constant velocity can usually fit the WB gather flatness in depth. In shallow 3D or 2D lines, either a WB depth velocity function or a TS-curve-derived function can be better used. Specific for shallow WB models, the CIG flatness can be checked using angle gathers generated from imaging with multiples, as will be mentioned later.

For the postsalt section, earlier model-building techniques used a simple starting velocity ( $V_0$ ) and gradient ( $k$ ) from well data. If the sonic well information is sparse or not evenly distributed over the area, then a smooth Dix interval velocity model (Dix, 1955) is inverted from a prestack time migration interval velocity and used as an initial model. In locations with known anisotropic parameters, an initial anisotropic model is built using area-specific Thomsen delta and epsilon values. If the anisotropic parameters are not confirmed from well information or the area includes variable compaction regimes not covered by well information, then the initial model is built for isotropic medium, followed by several isotropic tomography updates before the anisotropy is inserted.

With a few wavelet-shift vertical transverse isotropic (VTI) or tilted transverse isotropic grid tomography passes (Sherwood et al., 2011) performed over the initial model, the final postsalt section can be well imaged in depth. In the presence of the Pliocene gas sand channels, special interpretation for those bodies is required to separate the sand channels from the rest of the background velocity model. A variable  $Q$ -inverted model can be embedded to compensate for signal attenuation and dispersion. Full-waveform inversion (FWI) has been used to increase the velocity model contrast in the postsalt section by using both refractions and deeper backscattered energy in

the inversion (Brandesberg-Dahl et al., 2017). FWI methodology seeks to find a high-resolution, high-fidelity model of the subsurface that is capable of matching individual synthetic seismic waveforms with an original raw field data set. This is achieved iteratively by determining and minimizing a residual, or the difference between the modeled and recorded data. The model update is computed as a scaled representation of its gradient.

In the case of a shallow WB (less than 200 m), imaging with multiples (separated wavefield imaging [SWIM]) can be applied to enhance the resolution in the first few hundreds of meters below the WB (Lu et al., 2016; Whitmore, 2016). This can mitigate shallow hazards and derisk drilling location selection. It can also aid geologic, stratigraphic, and amplitude-variation-with-offset interpretation in certain situations. Migration of the multiples effectively creates “virtual” sources at each receiver position, enhancing subsurface illumination and resolution (Whitmore et al., 2010). This also effectively mitigates the “footprint” typically observed in wide-tow marine 3D seismic in shallow-water areas. The multiples illuminate the subsurface at smaller reflection angles than the primaries because the virtual sources are present along all receiver lines, not just the sparser shot lines. The angle gathers obtained from imaging using SWIM provide better near-angle, shallow illumination than the angle gathers obtained from Kirchhoff prestack depth migration (Figure 2).

The main challenge and the source of uncertainty in imaging the pre-Messinian section is the Messinian salt section. Figure 1 shows that the distribution of salt in the two major basins is interrupted by detrital deposits from the Nile Delta and other drainage systems. At the basin margins, the salt body geometry can change from simple horizontal bedding in a compressive regime to a more diapiric regime closer to the cone of the Nile Delta. Away from the diapiric region, in the Levant and Herodotus basins, the salt layer shows complex intrasalt reflectivity. Even though a constant velocity is assigned to that layer, it has surprisingly flattened the structure of the base of salt (BOS), as will be seen in the case studies. Also, a simple starting velocity and a gradient can best fit the pre-Messinian section up to the carbonate platform. Figure 3 shows a workflow that summarizes the velocity-model-building strategy in the eastern Mediterranean. In regions where the salt thins out

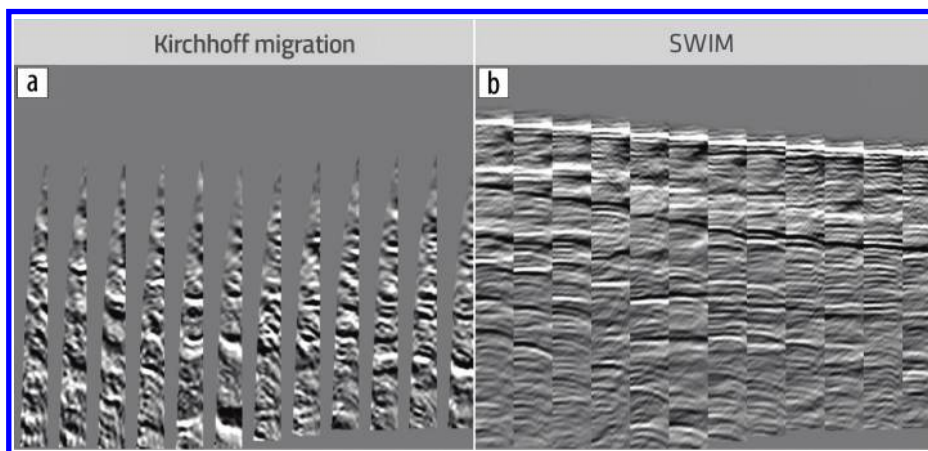


**Figure 2.** (a) Primary Kirchhoff  $45^\circ$  angle gathers with near-angle signal missing due to the wider angle of incidence of the primary energy on shallow reflectors. (b) SWIM wave-equation migration angle gathers up to  $45^\circ$  contain near-angle information.

to form local salt/anhydrite pockets, the starting model is analogous to the pre-Messinian section and will be followed by a series of focused tomography updates (El-Bassiony et al., 2016; Battistuti et al., 2018). This is the most complicated region to image the Messinian and the pre-Messinian sections. Other areas include salt with diapiric nature caused by tectonics that lead to inflow of the shales lying below the salt under the high pressure of trapped gas. Modeling of such complex intercalated shales/salt is one of the most challenging tasks for the interpreter. Therefore, a simple gradient model is assumed in such zones and tomography updates follow, while if the diapiric layer has a clear top and base salt, a simple constant velocity is used. Deeper in the section where the salt layer has a considerable thickness, a simple constant velocity for the salt is used, as well as a simple starting velocity and a gradient for the pre-Messinian. The Messinian thick salt layer velocity changes from 4200 m/s in the Herodotus Basin to 4300 m/s in the Levant Basin. The pre-Messinian flood velocity starts from 2400 m/s and progresses with a gradient  $k = 0.2$  m/s/m, where the detrital Miocene section is present. This starting velocity will increase to 2700–4000 m/s in locations characterizing the carbonate buildups that can reach the salt layer base. The model inside the carbonate buildups progresses with a relatively high gradient of 1.0–3.0 m/s/m, where the maximum velocity will be clipped at 5000 m/s.

The following sections present case studies for model building of the Messinian and pre-Messinian section from the Herodotus Basin offshore West Egypt to the Levant Basin offshore Lebanon, passing through the Cypriot waters and the ESM.

### Case studies

**Offshore West Egypt.** The PGS MultiClient data library includes 17,500 line km 2D offshore West Egypt and around 6000 km<sup>2</sup> 3D acquisition over the 2D data (Figure 4). The area is considered to be underexplored. It covers a narrow shelf zone including the south–north-trending Matruh Canyon in the south, a transform margin, and the Herodotus Basin and the Herodotus fold belt to the northwest.

The offshore West Egypt area has promising prospectivity, with the presence of proven Jurassic/Cretaceous oil and gas plays, Nile-sourced Pliocene sandstones, and potential presalt carbonate buildups analogous to the Zohr discovery.

The water layer is usually built after scanning the layer with constant water velocities. A final depth-dependent velocity function was used for the offshore West Egypt surveys. Building the Pliocene section in offshore West Egypt is challenged by the sparseness of well information. The Dix interval velocity inverted from prestack time migration velocity is smoothed spatially and used as an initial model. After a few tomography updates, a zero Thomsen's delta value was given for the whole model due to the absence of well information, and the epsilon value was scanned. The scans determined a good gradient model from the WB at epsilon = 0% to the top Messinian at 3%. The model was then enhanced by applying FWI updates. Figure 5 shows a deep water bottom (WB at 1.8 km) Pliocene section after two VTI tomography updates, then after 10 FWI VTI updates, and the FWI velocity update difference showing clear lower velocity trends at near-surface channels. The same figure shows a good FWI velocity update as deep as the Messinian top salt. The FWI model illustrates the high-velocity compact shales, lying just above the top salt, and an obvious geologically consistent trend across the major faults.

As an example of near-surface imaging in a shallow-water environment, SWIM was applied to 3D data offshore Nile Delta. Figure 6 shows the image uplift by using SWIM. The depth slice illustrates how acquisition footprint issues have been reduced. By using angles up to 45°, reflections down to 200 m including the WB reflector are better reconstructed in the SWIM image. Figure 7 shows the velocity model overlaying a prestack depth migration section from offshore Egypt in the Herodotus Basin. A constant interval velocity of 4200 m/s is applied within the whole Messinian salt (layer in yellow in Figure 7), approximating the whole intrasalt sediments with the clean salt and anhydrite average interval velocity.

The constant velocity model has provided flat BOS depth gathers globally across the Herodotus Basin (Figure 7). This velocity model can offer stable BOS structural trends and avoids uncertainty in perturbing the velocities inside the salt body. As the intrasalt events show very limited offset coverage, automatic picker-driven tomography constraints are challenged and will lead to some uncertainty. The large velocity contrast across the top-of-salt (TOS) surface causes deviations in the wavefield inside the salt. This deviation is more toward the horizontal plane,

making its incidence on any intrasalt event quickly reach critical angle, and only limited near-offset reflectivity from the intrasalt is recorded. Velocity errors inside the Messinian salt layer are partially obvious at the base salt structure, but will be clearer on the Serravallien and deeper Cretaceous sections, and can mislead the interpretation and volumetric studies. A model-uncertainty study can be applied inside the Messinian salt layer to explain velocity variation inside the Messinian section, creating different depth levels and undulations in the structure laterally, though keeping the CIG flat (Bell et al., 2016). Feng and Reshef (2016) show successful

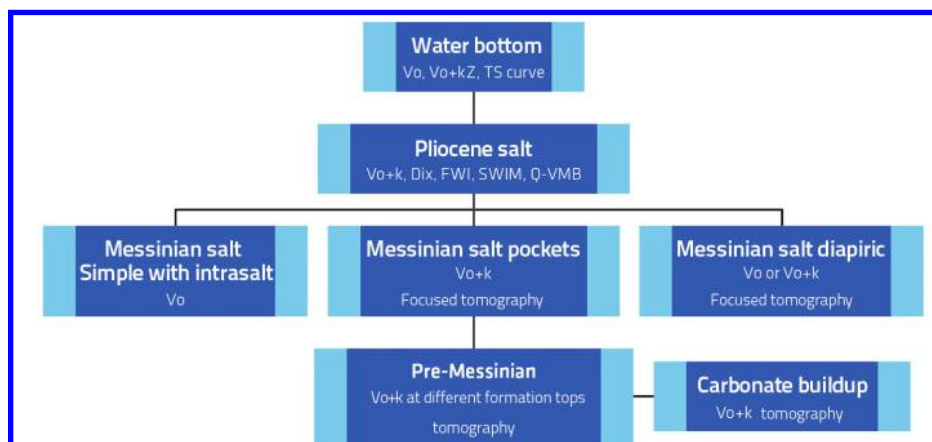


**Figure 3.** Workflow for the general strategy of velocity model building the Messinian salt in the eastern Mediterranean.

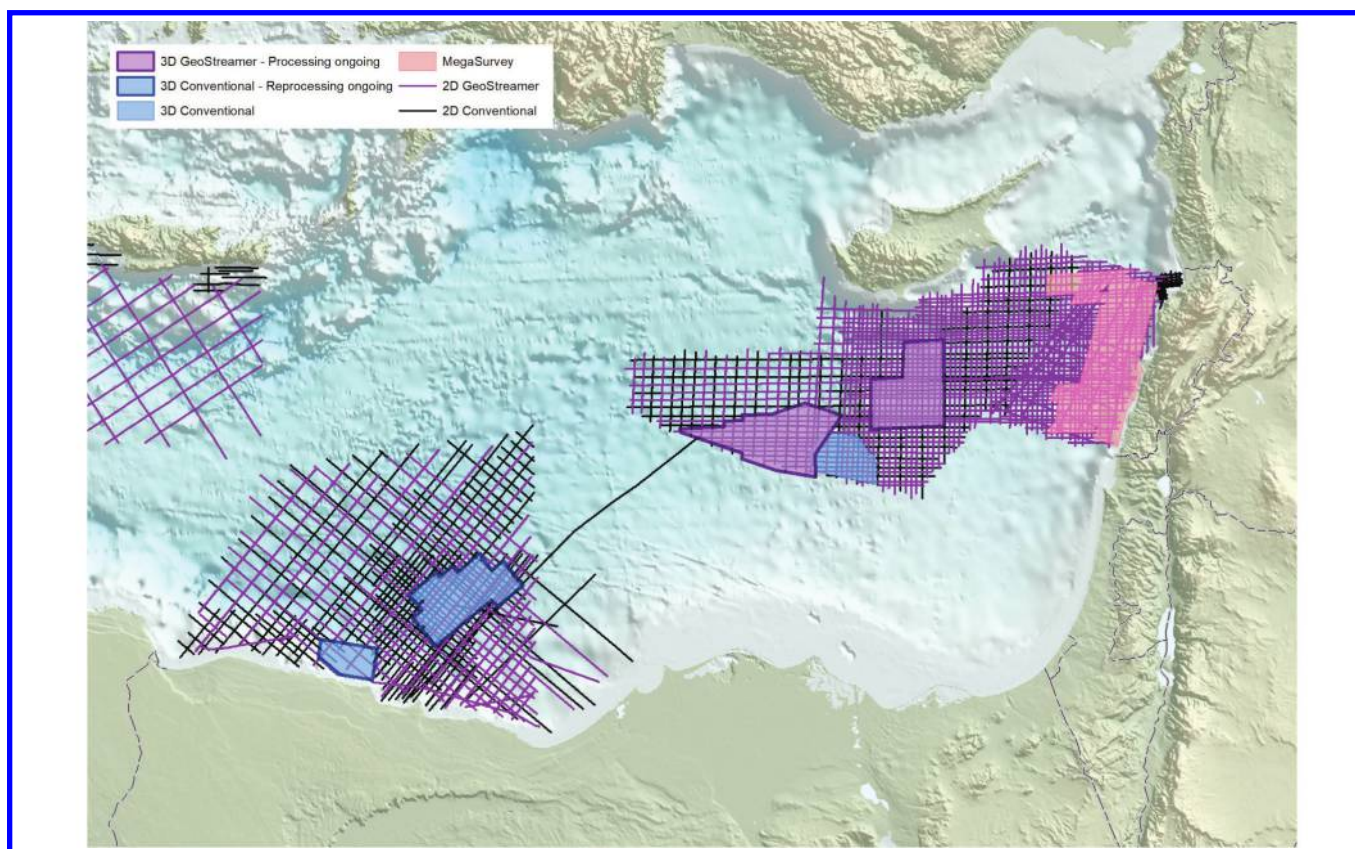


**Figure 4.** Eastern Mediterranean map showing the PGS 2D and 3D MultiClient data acquired using dual-sensor streamers and conventional acquisition (Widmaier and Lie, 2016).

tomography updates inside the salt layer that look superior to a constant velocity flood in areas south of the Levant Basin, but their results were not compared to reasonable equivalent constant average interval velocity value. Instead, the comparison was done with a far higher value of 4400 m/s. The Messinian salt layer has been studied in many concessions covering the Herodotus Basin and across the offshore Nile Delta to the Levant Basin in the west (North Leil, offshore Karawan, North Thekah, North Port Foad, and North El Arish). All studied locations reveal a good interval velocity for the salt that lies between 4200 and 4300 m/s.

The pre-Messinian section inside the Herodotus Basin, offshore West Egypt, starts with a 2400 m/s at the BOS and progresses with a gradient of 0.2 m/s/m. This simple model was enough to image the pre-Messinian globally up to 12 km depth. Velocity updates can be further performed, but the uplift in the global imaging quality will be marginal.

For mega 2D surveys, the final 2D model for each line is validated using mis-tie analysis with the rest of the intersecting lines and a robust algorithm is used to highlight important mis-tie locations. Mis-ties exist where there are difficulties in interpreting 2D lines in depth in a global sense. The final 2D models for all the processed lines were stretched to the time domain and interpolated to form a consistent and continuous 3D model. This was smoothed and stretched to depth, acting as a global stretching model for all the 2D lines to depth to achieve global line-to-line ties.

Other 3D surveys processed offshore West Egypt in the Herodotus Basin and close to the Levant Basin and ESM offshore Egypt proved to fit the same model of the Messinian

and pre-Messinian. The presence of the carbonate buildups closer to the ESM requires special surface picking and carbonate floods with 3600 m/s and a relatively high gradient to fit the gather flatness beneath.

An anomalous reflection beneath the BOS was always noted whenever a considerable salt thickness was encountered. Inspection of the arrivals of this ghost BOS reflection revealed a mid- to far-offset event with velocity close to 3100 m/s and bearing the same phase response as the BOS. By forward acoustic modeling using finite differencing methods of the PP-SP and PS-PP asymmetrical converted waves that travel inside the salt layer, it was evident that the asymmetric converted wave-modeled events matched the anomalous reflections (Kumar et al., 2018). Existing methods to suppress converted modes include filtering based on normal moveout velocity (Ogilvie and Purnell, 1996) or surgical muting of energy using traveltimes ray tracing (Lu et al., 2003). The presence of complex salt geometries imposes some limitations on these methods. Dual-leg 3D acoustic modeling was used to model converted waves (Huang et al., 2013), which was then used to attenuate it from the premigration or postmigration data set. In the presence of complex salt geometries, diffractions from the top salt cover the converted mode of the base salt modeled by forward modeling. This proves an additional challenge to subtraction in the data domain. Kumar et al. (2018) design a workflow to perform 3D acoustic modeling twice, with and without the base salt interface in the velocity model. This generates a much cleaner converted wave model that can be subtracted from premigration gathers. Figure 8

shows a 3D Nile Delta offshore example of modeling the converted wave. The modeled converted wave event was then adaptively subtracted from the input shots, and the migrated image reveals a cleaner subsalt image.

**Offshore Lebanon.** Offshore Lebanon can be subdivided into the northern part of the Levant Basin and the Levant Margin.

The Senonian unconformity marks the onset of clastic deposition onto Upper Cretaceous carbonates, which are predominantly present along the Levant Margin. Although the area remains underexplored with no wells drilled, data suggest the presence of all necessary components for a working petroleum system. Depth-migrated data show several structural closures in each of the

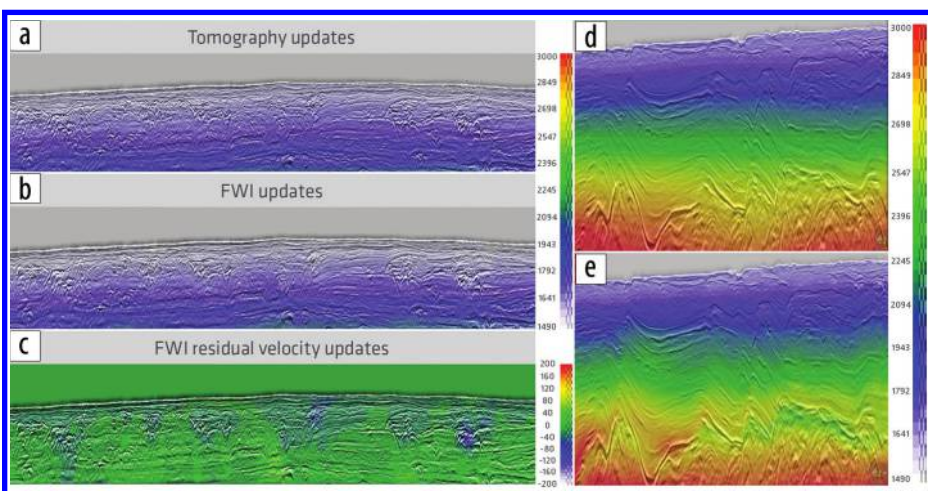


**Figure 5.** First three panels show deepwater offshore West Egypt 2D line. (a) Two global tomography updates in the Pliocene. (b) After 10 iterations of FWI using refraction and reflection data. (c) The residual velocities detected by the FWI updates. (d) Same 2D inline offshore West Egypt with input to FWI. (e) After 10 iterations of FWI updates to the top Messinian salt. The effect of the highly compacted shales just above the Messinian salt is obvious from the abrupt increase in velocities detected by the FWI updates showing good geologic tie-in.

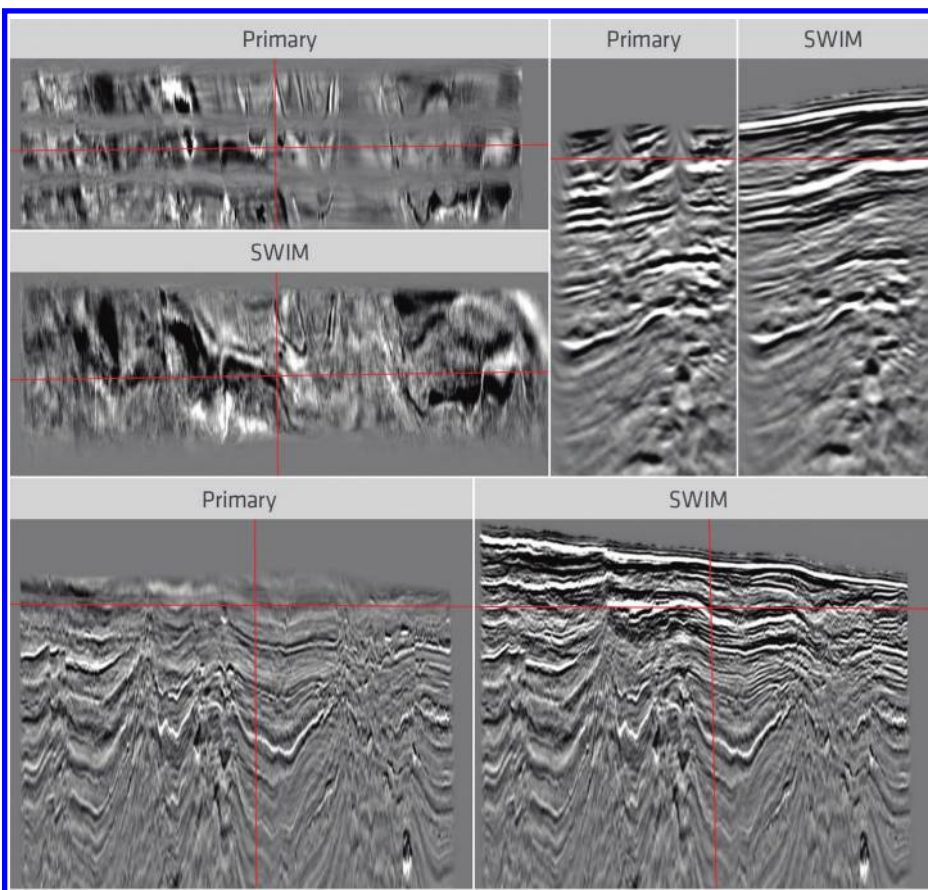


**Figure 6.** SWIM versus primary images in the shallow water offshore Nile Delta. Primary and SWIM images displayed at a 45° angle mute.

potentially prolific intervals in the area. The Messinian salt velocity was tested across a 2D survey that consists of more than 9000 line km of dual-sensor data and about 10,000 km<sup>2</sup> of 3D data (Figure 4).

The water layer velocity scans reveal a WB depth-dependent velocity function ( $V_0 + kZ$ ). The Pliocene section started with a smoothed Dix-inverted interval velocity model with anisotropy perturbed only within the epsilon model. Due to the absence of wells in the area, the delta model was set to 0% and the epsilon model terminated with a maximum value of 2% at TOS.

The Messinian salt layer showed a relatively higher interval velocity in the Levant Basin. A constant Messinian salt layer of 4300 m/s corrected the CIG flatness at BOS globally in the whole area. The Miocene section below the Messinian salt layer started with the characteristic 2400 m/s and a gradient of 0.2 m/s/m, analogous to the Herodotus Basin away from the continental shelf, while this gradient increased to 0.3 m/s/m as it approached the continental shelf region. The Senonian unconformity, marking the onset of the clastic deposition, was interpreted and used to embed a higher velocity of 4000 m/s to flatten the potential reservoirs of Cretaceous-Jurassic dolomites and sandstone events (Figure 9). To the east of the survey area, the continental shelf is characterized by the obvious thinning of the salt layer and the massive continental margin. This required a different starting velocity of 2700 m/s and a gradient of 1.8 m/s/m to adjust the CIG flatness in the continental shelf.

**Offshore Cyprus.** PGS MultiClient data for offshore Cyprus consist of more than 12,000 line km of 2D conventional and dual-sensor acquisitions. Two main surveys were shot in 2006 (conventional) and 2008 (dual sensor). The conventional survey maximum offset was limited to 8 km while the dual-sensor

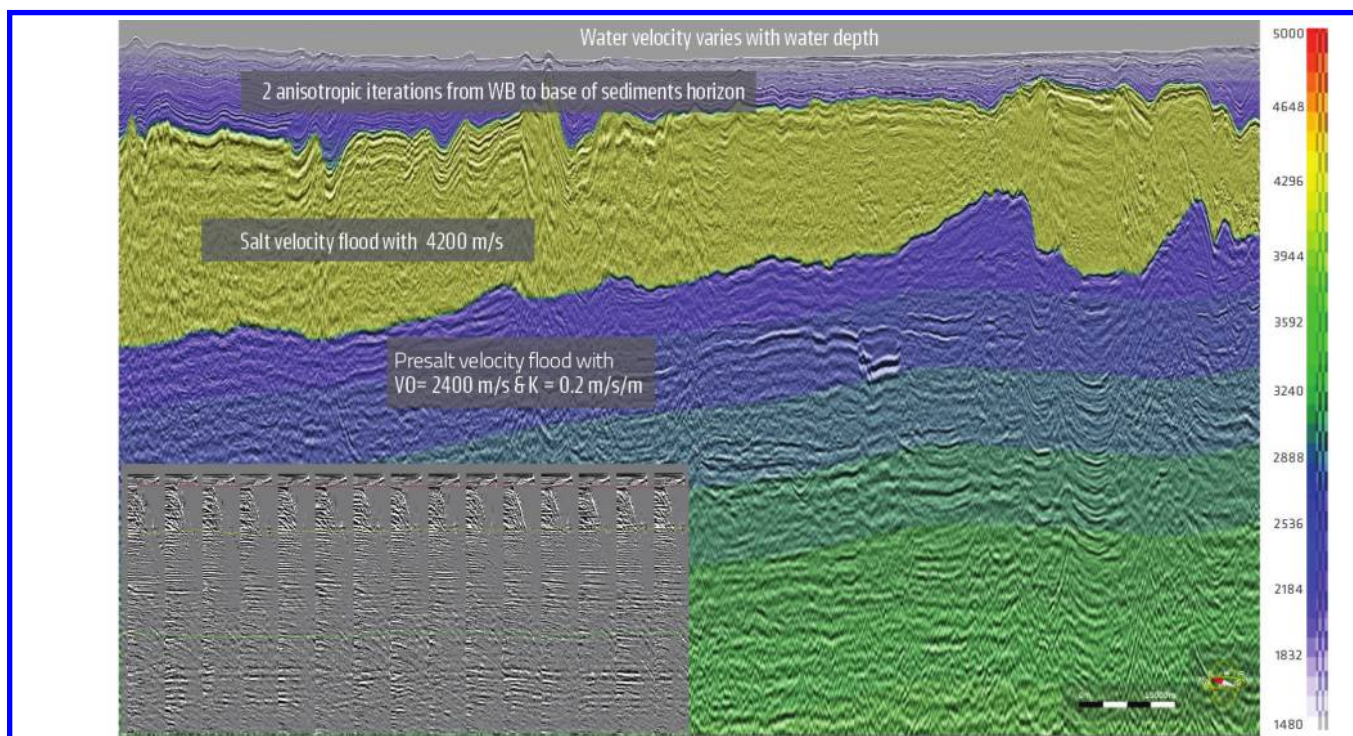


**Figure 7.** Egypt depth image and velocity overlay. Beam depth image with final vertical velocity model including Messinian salt layer with 4200 m/s and pre-Messinian section with  $V_0 = 2400$  m/s and gradient  $k = 0.2$  m/s/m.

survey was acquired with 10 km maximum offset. Figure 4 shows the location and distribution of the different acquisition surveys offshore Cyprus.

Water velocity scans performed offshore Cyprus revealed a water column velocity variation with WB depth. A  $V_0 + kZ$  model was used for the WB gather flatness. The relatively thin Pliocene section started with a Dix-inverted model adequately smoothed and updated through three to four iterations to ensure flat TOS gathers. A lack of well information forced the application of zero delta in the Pliocene section, but the epsilon parameter was inserted as a gradient model from the WB at 0% down to TOS with a maximum value reaching 2%. The insertion of a gradient epsilon model was required to flatten the far-offset events in the compacted shale layers just above the Messinian salt and away from the critical refracted arrivals, which persist at the TOS events.

Messinian salt velocity scans reveal a value of 4200 m/s for a global BOS structural flatness and also correct for the undulations in the pre-Messinian structures. Figure 10 shows a zoomed display of a broadband  $Q$ -compensated Kirchhoff image of the Messinian salt complex with clear intrasalt sequences. It is clear from the lower intrasalt member (which is assumed to bear a lower velocity than a clean salt from its characteristic top phase) that the BOS geometry is independent of the thickness of this lower intrasalt

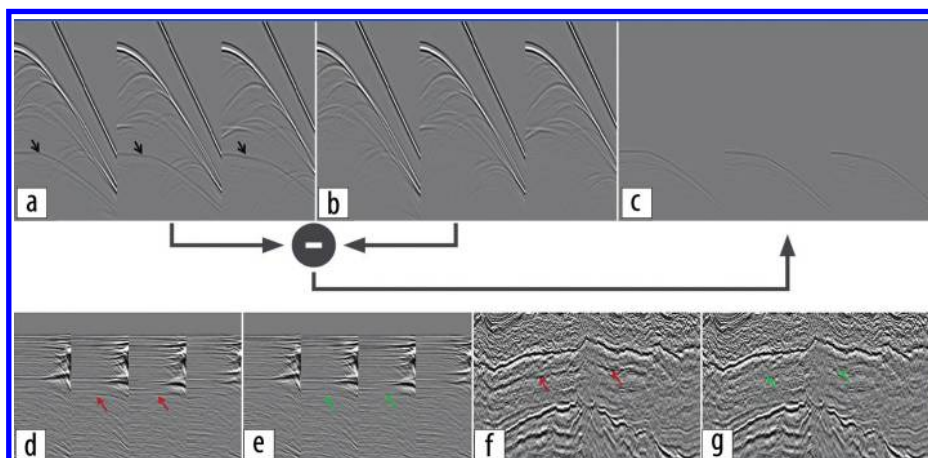


**Figure 8.** The upper panel shows different stages of modeling. (a) 3D acoustic forward modeling with base salt reflector included in the modeling. (b) Forward modeling without base salt reflector in the model. (c) Subtraction of the previous two models to generate clean converted wave model. The lower panel shows the image domain gathers (d and e) and stacks (f and g) using input data set without the converted wave-attenuation flow applied (d and f) and with the converted wave-attenuation flow applied (e and g). The image in this example has been produced using Kirchhoff depth migration.

member. Assuming that this lower intrasalt member has a consistent velocity lower than that of clean salt/evaporites, then the BOS would be expected to be a mirror image of its boundary, but this is not the case. In fact, it seems that the lower intrasalt thickness has been shaped by the dynamics of the inflow that provided the sediments for the original evaporites. Figure 10 shows no correlation between the pre-Messinian structure and the BOS structure regarding the layer dip and local BOS undulations, indicating complete success in removing the effect of the whole Messinian salt body. The pre-Messinian model started with

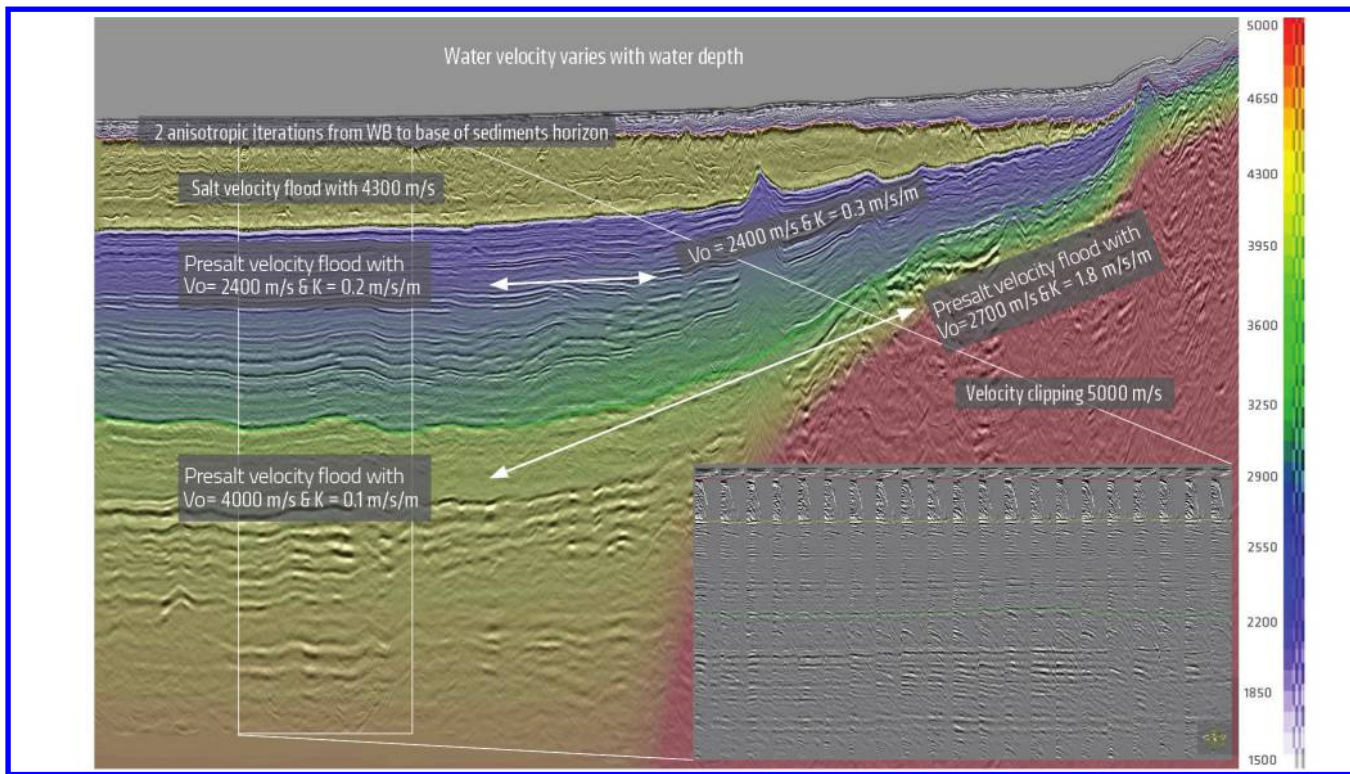


**Figure 9.** Lebanon depth image and velocity overlay. East–west-trending 2D beam depth image with final vertical interval velocity model showing a gentle TOS and BOS structure, with intrasalt sequence independent of the BOS geometry. Close to the shelf margin, the salt layer thins out and the presalt flood started with higher velocities and gradient.

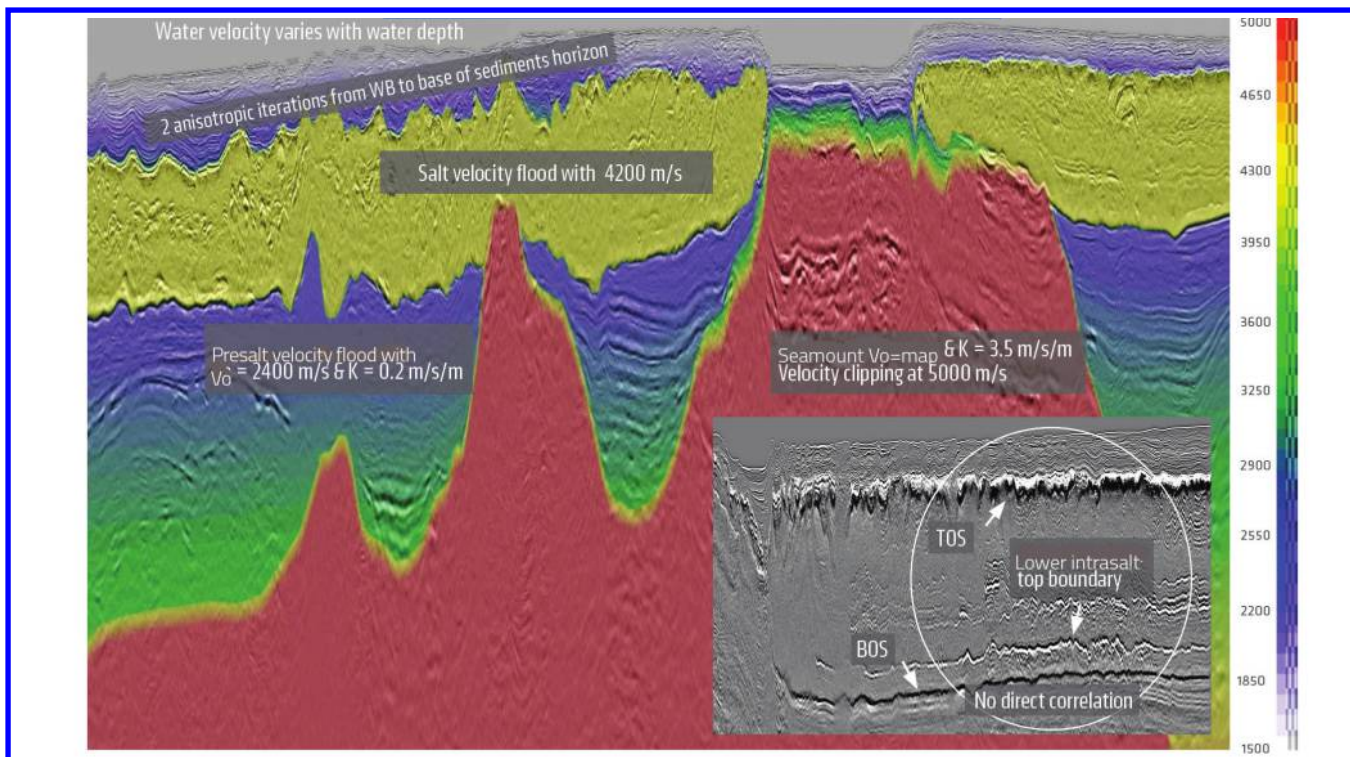


**Figure 10.** Cyprus depth image and velocity overlay. Final vertical velocity depth model over a beam depth image showing the pre-Messinian section and the carbonate buildups offshore Cyprus. The zoomed display shows a broadband Q-Kirchhoff depth image close to the ESM, showing details of the Messinian TOS and intrasalt sequences and their correlation to the BOS geometry using a constant flood velocity of 4200 m/s inside the whole Messinian salt layer.

the 2400 m/s and a gradient of 0.2 m/s/m. The pre-Messinian section close to the ESM showed a higher gradient of 0.3 m/s/m. The higher gradient in the pre-Messinian section can be justified by the increased compaction caused by the huge ESM tectonics. The carbonate buildups show a relatively higher starting velocity that is best derived by using a spatially variable velocity image from the overburden and progressing deeper with a high gradient of around 3.5 m/s/m and a clip velocity of 5000 m/s (Figure 10).

## Summary and conclusions

The Herodotus and Levant basins share many similarities in the nature of sedimentation and compaction regimes. Both basins include the same lithology with almost the same thicknesses. The deposition of the Messinian salt has globally introduced a thick layer of salt with some intrasalt sediment from the different drainage systems. The velocity model building of the Pliocene showed similar velocity profiles and similar anisotropic parameters, although the well information providing anisotropic parameters was limited in both basins. Shallow WB imaging can be enhanced using SWIM. FWI can be used to high grade the near-surface model by adding resolution that can be adequately checked using SWIM angle gathers.

The Messinian salt layer section shows the same similarities in the compressional wave velocities, regardless of the different complexities in their intrasalt sedimentation. Tomography updates inside the salt layer using traditional automatic picking is not recommended due to the weak constraints on the offset/angle coverage limitation for any reflectivity inside the salt layer. Model-uncertainty studies proved that the perturbation of the velocities inside the salt can be strong enough to deteriorate the base salt structure while keeping the gather flat at the BOS. This reflects the low confidence on moveout constraint for tomography within the salt.

The pre-Messinian section shows a more consistent starting velocity and gradient but requires a change in the gradient or the starting velocity whenever a carbonate is encountered. The Levant Basin shows the Senonian unconformity as a mark of an increased gradient to capture the compact and dense dolomites and sandstone layers beneath. In Cyprus and close to the ESM, the carbonate buildups have reached the Messinian salt in some locations, marked by an increase in the compressional wavefield velocities.

Finally, the velocity model building of the two major basins in the eastern Mediterranean can be achieved with relatively simple velocity-model-building techniques to image a globally correct pre-Messinian structure. Amplitude fidelity of the pre-Messinian section can be preserved if the salt layer geometry and velocities are accurately introduced. The structural integrity of the pre-Messinian section can be used to judge the degree of accuracy of the Messinian salt model build. Again, model-uncertainty studies can show that the uncertainties in the pre-Messinian section are lower than in the Messinian salt layer. This is due to the wider angle of coverage of the pre-Messinian events and therefore a relaxation on the data-driven constraints for tomography. Acquisition offset limitations and limited azimuth reduce constraints on the deeper tomography updates. Here, the importance of long offsets and rich azimuthal acquisition benefits model building and imaging beneath the complex Messinian salt. **TLE**

## Acknowledgments

The authors wish to thank PGS MultiClient for the authorization to show examples from the different surveys acquired by PGS throughout the eastern Mediterranean. Grateful thanks is also given to the PGS Cairo imaging team for providing the case studies. The authors wish to thank Aoife O'Mongain and Vinnie Papenfus from PGS MultiClient and an anonymous reviewer for their valuable edits to this paper.

Corresponding author: ahmed.elbassiony@pgs.com

## References

- Aal, A. A., A. El Barkooky, M. Gerrits, H. Meyer, M. Schwander, and H. Zaki, 2000, Tectonic evolution of the Eastern Mediterranean Basin and its significance for hydrocarbon prospectivity in the ultradeepwater of the Nile Delta: The Leading Edge, **19**, no. 10, 1086–1102, <https://doi.org/10.1190/1.1438485>.
- Battistutti, E., I. Mannino, and S. di-Benedetto, 2018, Improved subsurface imaging — Karawan and North Leil case history: Presented at 9<sup>th</sup> Mediterranean Offshore Conference.
- Bell, A. C., L. Russo, D. W. van der Berg, and T. Martin, 2016, Quantifying velocity model attribute uncertainty: A case study: Presented at 78<sup>th</sup> Conference and Exhibition, EAGE.
- Ben-Avraham, Z., A. Ginzburg, J. Makris, and L. Eppelbaum, 2002, Crustal structure of the Levant Basin, eastern Mediterranean: Tectonophysics, **346**, no. 1-2, 23–43, [https://doi.org/10.1016/S0040-1951\(01\)00226-8](https://doi.org/10.1016/S0040-1951(01)00226-8).
- Brandesberg-Dahl, S., N. Chemingui, and A. Valenciano, 2017, FWI for model updates in large-contrast media: Presented at 15<sup>th</sup> International Congress of the Brazilian Geophysical Society and EXPOGEF, 308–312.
- Dix, C. H., 1955, Seismic velocities from surface measurements: Geophysics, **20**, no. 1, 68–86, <https://doi.org/10.1190/1.1438126>.
- Druckman, Y., B. Buchbinder, G. M. Martinotti, R. S. Tov, and P. Aharon, 1995, The buried Afq Canyon (eastern Mediterranean, Israel): A case study of a Tertiary submarine canyon exposed in Late Messinian times: Marine Geology, **123**, no. 3-4, 167–185, [https://doi.org/10.1016/0025-3227\(94\)00127-7](https://doi.org/10.1016/0025-3227(94)00127-7).
- El-Bassiony, A., S. Butt, D. Cavalin, R. Ramadan, and H. Crook, 2016, Controlled sensitivity tomography for depth imaging the NAZ surveys in the Nile Delta's Messinian: Presented at 12<sup>th</sup> Middle East Geosciences Conference and Exhibition.
- Elia, C., P. Konstantopoulos, A. Maravelis, and A. Zelilidis, 2013, The tectono-stratigraphic evolution of eastern Mediterranean with emphasis on Herodotus Basin prospectivity for the development of hydrocarbon fields: Bulletin of the Geological Society of Greece, **XLVII**.
- Feng, Y. E., and M. Reshef, 2016, The eastern Mediterranean Messinian salt-depth imaging and velocity analysis considerations: Petroleum Geoscience, **22**, 333–339, <https://doi.org/10.1144/petgeo2015-088>.
- Gardosh, M., and Y. Druckman, 2006, Seismic stratigraphy, structure and tectonic evolution of the Levantine Basin, offshore Israel: GSL Special Publications, **260**, no. 1, 201–227, <https://doi.org/10.1144/GSL.SP.2006.260.01.09>.
- Gardosh, M., Y. Druckman, B. Buchbinder, and M. Rybakov, 2008, The Levant Basin offshore Israel: Stratigraphy, structure, tectonic evolution and implications for hydrocarbon exploration: Geophysical Institute of Israel Report 429.

- Garfunkel, Z., 1998, Constrains on the origin and history of the Eastern Mediterranean Basin: *Tectonophysics*, **298**, no. 1-3, 5–35, [https://doi.org/10.1016/S0040-1951\(98\)00176-0](https://doi.org/10.1016/S0040-1951(98)00176-0).
- Gradmann, S., C. Hübscher, Z. Ben-Avraham, D. Gajewski, and G. Netzeband, 2005, Salt tectonics off northern Israel: *Marine and Petroleum Geology*, **22**, no. 5, 597–611, <https://doi.org/10.1016/j.marpetgeo.2005.02.001>.
- Huang, Y., W. Gou, O. Leblanc, S. Ji, and Y. Huang, 2013, Salt-related converted-wave modelling and imaging study: 75<sup>th</sup> Conference and Exhibition, EAGE, Extended Abstracts, <https://doi.org/10.3997/2214-4609.20130356>.
- Kumar, J., M. Salem, and D. E. Cegani, 2018, A method to suppress salt-related converted wave using 3D acoustic modelling: Presented at 80<sup>th</sup> Conference and Exhibition, EAGE.
- Loncke, L., V. Gaullier, J. Mascle, B. Vendeville, and L. Camera, 2006, The Nile deep-sea fan: An example of interacting sedimentation, salt tectonics, and inherited subsalt paleotopographic features: *Marine and Petroleum Geology*, **23**, no. 3, 297–315, <https://doi.org/10.1016/j.marpetgeo.2006.01.001>.
- Lu, R. S., D. E. Willen, and I. A. Watson, 2003, Identifying, removing, and imaging P-S conversions at salt-sediment interfaces: *Geophysics*, **68**, no. 3, 1052–1059.
- Lu, S., N. Whitmore, A. Valenciano, N. Chemingui, and G. Ronholt, 2016, A practical crosstalk attenuation method for separated wavefield imaging: 86<sup>th</sup> Annual International Meeting, SEG, Expanded Abstracts, 4235–4239, <https://doi.org/10.1190/segam2016-13849878.1>.
- Macgregor, D. S., 2012, The development of the Nile drainage system: Integration of onshore and offshore evidence: *Petroleum Geoscience*, **18**, 417–431, <https://doi.org/10.1144/petgeo2011-074>.
- Netzeband, L. G., K. Gohl, P. C. Hübscher, Z. Ben-Avraham, G. A. Dehghani, D. Gajewski, and P. Liersch, 2006, The Levantine Basin — Crustal structure and origin: *Tectonophysics*, **418**, no. 3–4, 167–188, <https://doi.org/10.1016/j.tecto.2006.01.001>.
- Ogilvie, J. S., and G. W. Purnell, 1996, Effects of salt-related mode conversions on subsalt prospecting: *Geophysics*, **61**, no. 2, 331–348, <https://doi.org/10.1190/1.1443962>.
- Roberts, G., and D. Peace, 2007, Hydrocarbon plays and prospectivity of the Levantine Basin, offshore Lebanon and Syria from modern seismic data: *GeoArabia*, **12**, no. 3.
- Robertson, A. H. F., 1998, Tectonic significance of the Eratosthenes Seamount: A continental fragment in the process of collision with a subduction zone in the eastern Mediterranean (Ocean Drilling Program Leg 160): *Tectonophysics*, **298**, no. 1-3, 63–82, [https://doi.org/10.1016/S0040-1951\(98\)00178-4](https://doi.org/10.1016/S0040-1951(98)00178-4).
- Robertson, A. H. F., and D. Mountrakis, 2006, Tectonic development of the eastern Mediterranean region: An introduction, *in* A. H. F. Robertson and D. Mountrakis, eds., *Tectonic development of the eastern Mediterranean region: GSL Special Publications* **260**, 1–9.
- Sherwood, J., J. Jiao, H. Tieman, K. Sherwood, C. Zhou, S. Lin, and S. Brandsberg-Dahl, 2011, Hybrid tomography based on beam migration: 81<sup>st</sup> Annual International Meeting, SEG, Expanded Abstracts, <https://doi.org/10.1190/1.3628037>.
- Voogd, B., and C. Truffert, 1992, Two-ship deep seismic soundings in the basins of the eastern Mediterranean Sea (Pasiphae cruise): *Geophysical Journal International*, **109**, no. 3, 536–552, <https://doi.org/10.1111/j.1365-246X.1992.tb00116.x>.
- Whitmore, N., 2016, Extending the 3D primary image with multiples and mirrors: 86<sup>th</sup> Annual International Meeting, SEG, Expanded Abstracts, 4901–4905, <https://doi.org/10.1190/segam2016-13873954.1>.
- Whitmore, N. D., A. A. Valenciano, W. Sollner, and S. Lu, 2010, Imaging of primaries and multiples using a dual-sensor towed streamer: 80<sup>th</sup> Annual International Meeting, SEG, Expanded Abstracts, <https://doi.org/10.1190/1.3513508>.
- Widmaier, M., and Ø. Lie, 2016, Experiences with dual-sensor towed streamer acquisition and imaging in the eastern Mediterranean: Presented at 12<sup>th</sup> Middle East Geosciences Conference and Exhibition.